

N75-15940

**NASA TECHNICAL
MEMORANDUM**

NASA TM X-72646

NASA TM X-72646

DESCRIPTION AND EVALUATION OF THE VIKING LANDER CAMERA

PERFORMANCE PREDICTION PROGRAM

By Friedrich O. Huck, Edward J. Taylor,
Daniel J. Jobson, and Carroll W. Rowland

January 1975



This informal documentation medium is used to provide accelerated or special release of technical information to selected users. The contents may not meet NASA formal editing and publication standards, may be revised, or may be incorporated in another publication.

**NATIONAL AERONAUTICS AND SPACE ADMINISTRATION
LANGLEY RESEARCH CENTER, HAMPTON, VIRGINIA 23665**

1. Report No. TM X-72646	2. Government Accession No.	3. Recipient's Catalog No.	
4. Title and Subtitle DESCRIPTION AND EVALUATION OF THE VIKING LANDER CAMERA PERFORMANCE PREDICTION PROGRAM		5. Report Date January 1975	
7. Author(s) Friedrich O. Huck, Edward J. Taylor, Daniel J. Jobson, and Carroll W. Rowland		6. Performing Organization Code	
9. Performing Organization Name and Address NASA Langley Research Center Hampton, Virginia 23665		8. Performing Organization Report No.	
12. Sponsoring Agency Name and Address National Aeronautics and Space Administration Washington, D.C. 20546		10. Work Unit No.	
15. Supplementary Notes		11. Contract or Grant No.	
		13. Type of Report and Period Covered Technical Memorandum	
		14. Sponsoring Agency Code	
16. Abstract A computer program is described for predicting the performance of the Viking lander cameras. The predictions are primarily concerned with two objectives: (1) the picture quality of a reference test chart (of which there are three on each lander) to aid in diagnosing camera performance; and (2) the picture quality of cones with surface properties of a natural terrain to aid in predicting favorable illumination and viewing geometries and operational camera commands. Predictions made with this program are verified by experimental data obtained with a Viking-like laboratory facsimile camera.			
17. Key Words (Suggested by Author(s)) (STAR category underlined) Image quality Viking lander camera 14	18. Distribution Statement Unclassified - Unlimited		
19. Security Classif. (of this report) Unclassified	20. Security Classif. (of this page) Unclassified	21. No. of Pages 49	22. Price* \$3.75

*Available from { The National Technical Information Service, Springfield, Virginia 22151

STIF/NASA Scientific and Technical Information Facility, P.O. Box 33, College Park, MD 20740

DESCRIPTION AND EVALUATION OF THE VIKING LANDER CAMERA

PERFORMANCE PREDICTION PROGRAM

By Friedrich O. Huck, Edward J. Taylor
Daniel J. Jobson, and Carroll W. Rowland

SUMMARY

A computer program is described for predicting the performance of the Viking lander cameras. The predictions are primarily concerned with two objectives: (1) the picture quality of a reference test chart (of which there are three on each lander) to aid in diagnosing camera performance; and (2) the picture quality of cones with surface properties of a natural terrain to aid in predicting favorable illumination and viewing geometries and operational camera commands. Predictions made with this program are verified by experimental data obtained with a Viking-like laboratory facsimile camera.

INTRODUCTION

Two Viking spacecraft scheduled to land on Mars in 1976 will each use two facsimile cameras to spatially, radiometrically, and spectrally characterize the surface. The cameras feature a photosensor array with 12 silicon diodes to provide a variety of imaging modes, including six spectral bands for color and near-infrared imaging with an angular resolution of 0.12° , and 4 focus steps for monospectral imaging with an improved angular resolution of 0.04° . The field of view in elevation ranges from 40° above to 60° below the horizon, and in azimuth is selectable in 2.5° steps up to 342.5° . High sensitivity is obtained over a wide dynamic range with only 6-bit

encoding by use of 6 linear gains and 32 offsets. The camera scanning rates are synchronized to the lander data transmission rates of 16,000 bits per second to two orbiters as relay stations and 250 bits per second directly to Earth.

The versatility of these cameras demands a carefully designed imaging strategy to optimize their use. The strategy for the first few pictures must be based on pre-flight predictions of image quality as a function of anticipated Mars surface properties and illumination and viewing geometry as well as on camera characteristics. Thereafter, the strategy can be determined with the help of the initial pictures.

If the quality of the initial pictures received from Mars concurs generally with pre-flight predictions, then the basic pre-flight imaging strategy may be essentially continued for the subsequent investigations. If, however, the quality of the pictures is degraded either because the cameras are not performing properly or because the actual Mars optical environment departs significantly from anticipated characteristics, or because both situations occur, then the pre-flight imaging strategy may be of little further use. A flexible camera performance prediction computer program can aid first as a diagnostic tool in isolating the cause of picture degradation, and thereafter as a predictive tool in revising the imaging strategy. This diagnostic and predictive function can be accomplished in the following way: If the pictures obtained from viewing one of the reference test charts on the lander agrees with predictions, then the unexpectedly poor pictures of the scene must have been caused by differences between the actual and the anticipated Mars environment. However, if the pictures of the reference test chart do not agree with predictions, then the poor pictures must have been caused, at

least in part, by a degradation in camera performance. (But this latter situation would not preclude a significant difference between the anticipated and encountered environment). Whatever the inspection of the initial pictures and the camera engineering data may reveal, the resultant conjectures about degraded camera performance and unanticipated scene characteristics can be entered into the computer by altering pertinent camera and scene parameters until computational results come into agreement with the initial picture data. Thereafter, the computer program can again be used to predict favorable illumination and viewing geometry and camera control settings.

Suitable definitions and mathematical formulations of image quality criteria were derived in reference 1. This paper describes the camera performance program that has been developed from these criteria, and presents comparisons between predictions and experimental results obtained under controlled laboratory conditions. The experimental measurements were made with a laboratory facsimile camera that is similar in performance to the Viking lander cameras.

SYMBOLS

- b normalized diameter of approximated circular area of a cone section, pixels
- c normalized diameter of cone base, pixels
- D diameter, meters
- E electronic frequency response
- f lens focal length, meters
- g phase angle (see figure 6), degrees
- G gain of summing amplifier

I	current, amperes
I'	signal current normalized to $\phi(\epsilon, \iota, g) = 1$, amperes
i	integer
J_1	first order Bessel function
k	spatial frequency, line pairs per meter
k_c	camera calibration factor
k_p	camera optics factor
k_v	conversion factor between time and spatial frequencies
K	width of line pair of reference test chart tribars, meters
L	distance from camera lens in object space, meters
$L(u, s)$	lens spatial frequency response
λ	distance from camera lens in image space, meters
N	number of pixels in a cone section
N_λ	spectral radiance, watts/meter ² -micrometer-steradian
\hat{N}	unit vector normal to surface
n	number of overlapping line scans
$P(v_a s)$	spatial frequency response of circular photosensor aperture
P_λ	spectral radiant power, watts/micrometer
Q	quantitization level
r	reflectance
R_f	preamplifier feedback resistance, ohm
R_λ	photosensor responsivity, amperes/watt
S_λ	solar irradiance above Martian atmosphere, watts/meter ² -micrometer
S/N	ratio of average signal to root-mean-square noise
SNR	signal-to-noise ratio reference
s	dimensionless variable for spatial frequency k

u	dimensionless variable for defocus
v	dimensionless variable for radius
V	voltage, volts
V'	signal voltage normalized to $\phi(\epsilon, \iota, g) = 1$, volts
Z	cone geometry factor
α	target slope, degrees or radians
β	instantaneous field of view or angular resolution, degrees or radians
δ	azimuth cone angle increment, degrees or radians
ϵ	angle between emitted radiation and normal to surface (see figure 6), degrees or radians
ζ	azimuth angle between object slope and incident radiation (see figure 6), degrees or radians
θ	azimuth angle between incident and emitted radiation (see figure 6), degrees or radians
ι	angle between incident radiation and normal to surface (see figure 6), degrees or radians
κ	number of pixels per line-pair width of tribars
λ	wavelength, micrometer
Λ	wavelength integral
ρ_λ	spectral reflectivity of surface (normal albedo)
$\tau_\lambda(\iota_o)$	spectral transmissivity of atmosphere
τ_λ	optical throughput
ν	frequency, Hertz
ϕ	illumination scattering function
ψ	azimuth angle between object slope and emitted radiation (see figure 6), degrees or radians

Subscripts:

a photosensor aperture
c camera
e electronics
i integer
l lens
m mirror
n noise
o flat surface
q quantization
w window
+ brighter than flat surface
- darker than flat surface

The symbol Δ in front of a parameter indicates a peak or peak-to-peak variation of that parameter. The bracket < > around a parameter indicates a criterion which is to be estimated.

IMAGE QUALITY CRITERIA AND PREDICTION PROGRAM

Image quality criteria that have been formulated in reference 1 are briefly reviewed, and the computer program that is based on these criteria is described. It should be pointed out in order to avoid possible confusion that some details of the formulations obtained from reference 1 have been changed, and that formulations pertaining to the reference test chart have been added.

Image Quality Criteria

The Viking lander camera has four imaging modes: survey, high-resolution, color, and near infrared (IR). In the broad-band survey and high-resolution imaging modes, it is generally desirable to record small spatial details and slope variations. In the narrow-band color and IR imaging modes, it is generally desirable to record spectral variations. In addition, it is generally also desirable in all four imaging modes to encompass, but not exceed, the complete range of radiance variations in the scene with a single dynamic gain setting. Imagery of the reference test charts on each lander provides data for checking and calibrating the performance of the camera.

Broad-band imagery. - The capability to resolve small spatial details and slopes has been defined as the minimum detectable cone diameter and cone slope with respect to a level surface. A right-circular cone with surface properties of the surrounding terrain seems intuitively representative of many features and has no preferred surface orientation azimuthally about its axis. If the cone angle is chosen to be steep, a condition yielding high surface contrast, then the detectability of this target becomes primarily a measure of the camera capability to resolve small detail. If the cone angle is chosen to be shallow, a condition yielding low surface contrast, then the detectability of the same target becomes primarily a measure of the camera capability to resolve small slopes.

The cone is probably also the simplest shape for this application. But it would, nevertheless, be unnecessarily complex to translate rigorously cone-surface-radiance variations into image grey-scale variations in order to estimate the detectability of a cone. Instead, the average radiance is calculated separately over those regions of the cone which are brighter than

a level surface background, and those regions, including a shadow (if present), which are darker than the background. The two average reflectance values and their corresponding areas are then used as approximate target characteristics in order to formulate an expression for the average-signal-to-rms-noise ratio of the cone image.

Narrow-band imagery. - The capability to resolve spectral variations has been defined as the minimum detectable albedo variation. This minimum detectable variation is taken to be that difference in albedo which results in an average-signal-to-rms-noise ratio of 3, a level surface being assumed.

Dynamic range. - Knowledge of the statistical distribution (histogram) of surface radiance would allow the selection of optimum camera dynamic range setting (that is, gains and offsets as illustrated in Appendix A) for the complete or a desired part of the radiance range. But the actual radiance distribution will, of course, not be known until after data have been received from the lander. It has, therefore, been proposed that a minimum, mean, and maximum value of the radiance distribution be estimated, the albedo and illumination scattering function of the scene being assumed to be uniform over the landing site. Clearly, the minimum surface radiance occurs in shadows. Since atmospheric scattering on Mars is small (excepting, of course, during a dust storm) within the spectral range of the camera silicon photosensors, shadows will exhibit negligible radiance. Hence, for the purpose of selecting a camera offset, minimum radiance may be defined as zero. The mean radiance is defined as the radiance of a level surface for a given viewing geometry. The maximum radiance is defined as the radiance of a surface area with a slope and slope orientation which produces highest surface reflectance, again for a given viewing geometry.

Reference test chart imagery. - The reference test chart (see Appendix C) provides 11 grey scales to calibrate the radiometric response and 3 sets of tribars to check the frequency response of the camera; in addition, it provides three color patches to aid the construction of color images.

Camera Performance Prediction Program

Figure 1 presents a block diagram of the camera performance prediction program with all pertinent equations. The program is divided into three basic parts: input data, interface relations, and camera performance or image quality computations. The latter, in turn, can be divided into three sections: image quality of the reference test chart, and narrow-band and broad-band image quality of the scene.

Input data. - The input data consists of camera characteristics, spatial and reflectance data of the reference test chart, optical data of the environment, and illumination and viewing geometry. All of this data must be readily interchangeable during mission operations. But since the process of modification is primarily a computer interface function, it is not further discussed here. The input data used in this paper to evaluate image quality computations are given in appendices as follows:

1. Appendix A presents a description of the laboratory facsimile camera that is used in the experiments. The performance characteristics of this camera are similar to those of the Viking lander cameras.
2. Appendix B presents the irradiance characteristics of the National Bureau of Standard (NBS) lamp and the floodlight used as light sources for the experiments.
3. Appendix C presents spatial and reflectance characteristics of the

of the Viking reference test chart.

4. Appendix D presents pertinent characteristics of the surface material used for the broad-band image quality experiments, and the Meadow-Weaver illumination scattering function (ref. 2) that describes the diffuse reflectance of this material as a function of its physical properties such as particle size, single-particle albedo, and compactness.

Interface relationships. - The interface relationships primarily translate the input data and camera commands into quantities and units used by the image quality computations.

The more important computations are:

1. Most wavelength-dependent integrations, including in particular those integrations that are required to determine the surface radiance and camera response weighted average wavelength, $\bar{\lambda}$, the photosensor signal current, I' , and preamplifier output voltage, V' , normalized to $\phi(\epsilon, \lambda, g) = 1$.

2. Normalized camera parameters for the photosensor aperture radius, v_a , and defocus, u .

3. The conversion factor k_v between the time frequency, v , of electrical filters and spatial frequency, s , of optical filters.

4. The camera selectable dynamic range, which extends from V_{\min} to V_{\max} , as determined by the offset and gain commands. (The factor 0.216 is a constant negative offset in the video electronics).

5. The total camera rms noise, V_n , which consists of the photosensor array electronic noise, V_e , and the quantization noise, V_q . The effective electronic noise bandwidth BW is reduced by the factor n if a line is repeatedly scanned n times.

6. The overall electronic frequency response, $E(v)$, is the product of the frequency response of the photosensor preamplifier, $E_1(v)$, the analog video electronics, $E_2(v)$, and the running mean integrator used for analog-to-digital conversion; the integration time is $t_s/2$, and t_s is the time between samples.

Image quality: reference test chart. - The spectral radiance, $N_{\lambda,r}$, of the reference test chart and the spectral power falling on the photosensor are computed, assuming the illumination scattering function of the target to be Lambertian and the viewing angle normal. The results lead directly to the computation of the photosensor signal current, preamplifier output voltage, and digital data level. Computations for the tribar peak-to-peak signal account also for the frequency response of the lens, pinhole, video electronics, and sampling process. The frequency response computation includes the first three terms of the square-wave amplitude response as a function of the camera sine-wave frequency response. The sampling process generates a signal which is statistical rather than deterministic in nature. The factor $\frac{\sin\pi/k}{\pi/k}$ accounts for an average reduction in signal contrast; the actual signal may have a slightly higher or lower contrast.

Image quality: broad-band. - A cone with a normalized base diameter c (i.e., the actual diameter divided by the pixel diameter) and slope α has been selected to represent small spatial details or slopes. The program will compute either one of three alternatives: (1) If both α and c are given, the program will compute the resultant signal-to-noise ratio. (2) If only α is given, it will compute the minimum detectable cone diameter, that is, that value of c which results in a signal-to-noise ratio of SNR; SNR is an input based on experimental evaluations. (3) If only c is given, it will

compute the minimum detectable cone slope. Several computational iterations are required for the last two alternatives.

The first step is to compute the average value of the illumination scattering function over those regions of the cone which are brighter than a level surface background (ϕ_+), and those regions, including a shadow (if present), which are darker than the background (ϕ_-). Several lighting and viewing geometries must be carefully accounted for when computing the cone geometry factor Z , as explained in detail in reference 1. The second step is to compute the areas of the brighter and darker than background cone surface; these areas are then assumed to be circular with a normalized signal excursion of these two circular areas, B_+ and B_- , in order to account for the camera frequency response (including defocus blur).

Together with the previously computed normalized signal voltage V' , these results lead directly to the signal excursion ΔV_+ and signal-to-noise ratio S/N. If both α or c are given, then this signal-to-noise ratio is printed out. If either α or c are given, then a test is performed to determine if the signal-to-noise ratio is approximately equal to SNR. If not, then a value of α or c is estimated and all computations are repeated. Reiterations are performed until the value of α or c results in a signal-to-noise ratio approximately equal to SNR.

Image quality: narrow-band. - The noise-equivalent radiance and the minimum detectable albedo difference are directly computed from previously obtained results.

COMPARISON OF COMPUTER PREDICTIONS AND EXPERIMENTAL MEASUREMENTS

Two parts of the image quality prediction program need to be confirmed by experimental measurements; namely, the formulations that are concerned with the reference test chart and the cone targets. All other formulations contained in the program are either conventional or very simple, and the computer program of the formulations has been checked by independent computations.

It is of considerable interest to determine the agreement that can be obtained between predictions and experimental results under carefully controlled laboratory conditions. This agreement depends, of course, not only on the accuracy of the formulations but also on the accuracy with which camera and target characteristics are known. This limitation includes, in particular, the illumination scattering function of the basalt material used for the cone targets (see Appendix D).

Reference Test Chart Images

Predictions are compared to experimental results for four reference test chart pictures. The facsimile camera was located 1.0 m from the chart and viewed it normally ($\epsilon_0 = 0^\circ$). A NBS lamp (EPI 1577) was located 60 cm from the chart and illuminated it at an angle of 20° from normal ($\iota_0 = 20^\circ$). Three of these images are shown in figure 2: the first image was obtained in the so-called Hi-Res 1 mode, which has an instantaneous field of view of 0.044° and in-focus distance of 1.9 m; the second image was obtained in the Hi-Res 2 mode, which has the same instantaneous field of view but an in-focus

distance of 2.7 m; and the third image was obtained in the Survey mode, which has an instantaneous field of view of 0.132° and an in-focus distance of 3.7 m. A fourth image (not shown) was obtained in the color mode, which has the same instantaneous field of view and in-focus distance as the Survey mode but uses a red, green, and blue filter during alternating line scans.

Image details of the three tribars are particularly interesting because they reveal much about the overall camera performance. The large tribar is distinctly reproduced in all three imaging modes. Contrast of the medium tribar is slightly reduced in the Hi-Res 1 mode, significantly reduced in the Hi-Res 2 mode, and reduced to near the threshold level in the Survey mode. The smallest tribar is resolved at a very low contrast in the Hi-Res 1 mode, and gives rise to a so-called false resolution in the other two modes (i.e., in this case two rather than three bars).

Table I presents a listing of predicted and measured signal values for one of the grey patches, the three color patches, and the three tribars. The good agreement between predictions and measurements for the grey patch (4 percent on the average) results essentially from the fact that both camera and reference test chart reflectance calibrations have been made relative to magnesium carbonate ($Mg CO_3$), using the same NBS lamp. The slightly less favorable agreement for the color patches (15 percent for red and 7 percent for green and blue, on the average) results from the fact that accurate absolute reflectance measurements have not been made yet for these patches. It may be concluded that predictions of the radiometric throughput of the camera are accurate to within 10 percent, which is near the accuracy of the absolute radiometric calibrations of the Viking lander cameras.

The agreement between predicted and measured tribar contrast is better for the largest tribar (9 percent on the average) than for the two smaller tribars. The reason for the poorer agreement for the smaller tribars is easiest explained with the aid of figure 3, which presents the predicted camera square-wave frequency response and the normalized measurements of the tribar contrasts. It can be seen that the fundamental tribar frequency components near the steep slope of the curve and near zero result in the largest percentage disagreements. Such disagreements can readily result from small errors in camera focus adjustments, camera-to-target distance measurements, and tribar widths. It should be observed in particular that the combination of highest camera defocus blur and smallest tribar does not lead to the largest percentage disagreement since the fundamental tribar frequency component occurs at a shallow inflection rather than steep slope of the camera frequency response curve. Nevertheless, predictions and measurements agree sufficiently well so that any appreciable image contrast degradation caused by a camera problem can be effectively simulated.

Cone Images

Figure 4 presents a typical image of a cone, and a computer printout of the same data which gives the quantization level of each picture element (pixel). The signal-to-noise ratio of a cone is evaluated from this experimental data as follows: First, the evaluator outlines the part of the cone that is brighter than the background and the other part that is darker (including shadow, if present). Second, he records the number of pixels, N_{+} , in each section as well as their quantization levels, Q_{+} . The effective diameter of each cone section is taken to be

$$b_{\pm} = \sqrt{\frac{4}{\pi} N_{\pm}}$$

and the average signal excursion is

$$\Delta V_{\pm} = \frac{k_q}{N_{\pm}} \sum_{i=1}^{N_{\pm}} |Q_i - Q_o|$$

where Q_o is the background quantization level, and k_q the conversion factor from quantization level to signal voltage; $Q_i > Q_o$ for ΔV_+ , and $Q_i < Q_o$ for ΔV_- . Finally, the average-signal-to-rms-noise ratio is given by the expression (ref. 1)

$$\frac{S}{N} = \frac{\Delta V_+ + \Delta V_-}{V_n} \sqrt{b_+^2 + b_-^2}$$

where V_n is the rms value of the noise.

The evaluator has to make somewhat subjective judgments during the first step of the experimental evaluation whether or not he should include a pixel along the boundary of the cone image as part of the cone. Errors in judgment can be expected to lead to small errors in the final results for cone images which contain many pixels (200 or more) as shown in figure 4; however, the evaluation of such cones is very tedious. Cone images containing few pixels (20 to 80) were therefore independently evaluated by three persons to characterize typical variations in experimental results that are introduced by their different judgments. Results presented in figure 5 show a typical spread of experimental results. On the basis of these results, it was decided to evaluate a few pictures with (1) a single cone that contains many pixels (about 300) to make accurate comparisons for a few representative cases, and

(2) several cones that contain fewer pixels (about 40) per cone to check on proper trends of the variations of predicted signal-to-noise ratios with a variety of cone slopes and illumination and viewing geometry. A defining diagram of the illumination and viewing geometry is shown in figure 6.

Figure 7 presents three large cone images together with predicted and experimental results. Interesting intermediate results are the number of pixels contained in the brighter and darker-than-background parts of the cone, N_{+} ; the final result is signal-to-noise ratio, S/N . Results indicate that the experimentally determined signal-to-noise ratios tend to be slightly higher than the predicted values.

Figure 8 presents signal-to-noise ratio predictions and experimental results for seven cones with equal base diameters (3 cm) but different slopes (5° to 40°). The incident ($\iota_o = 70^\circ$) and emission ($\varepsilon_o = 60^\circ$) angles were kept constant, while the azimuth angle (θ) between illumination and viewing direction was varied in four steps from 45° to 180°. The average distance from the camera to the cones was 1.4 m; the exact distance of each cone from the camera was not accounted for in the predictions. As can be seen, the predictions are in consistently good agreement with the experimental results, at least within the accuracy to which the experimental data can be quantitatively reduced.

CONCLUDING REMARKS

A computer program for predicting the performance of the Viking lander cameras has been described, and predictions from this program have been compared with experimental results. The predictions were concerned with pictures of a reference test chart and of cones covered with natural (basalt)

material. Predictions of the picture quality of selected reference test chart features can aid in diagnosing camera performance. Predictions of the picture quality of cones with surface properties of natural terrains can aid in determining favorable lighting and viewing geometry and operational camera commands.

Predictions of the picture quality of selected reference test chart features were compared with experimental results for several camera imaging modes, providing different angular resolutions, defocus blur, and spectral responses. The predictions and measurements for the radiometric throughput of the camera generally agreed within 10 percent, which is near the expected accuracy of the absolute radiometric calibration of the Viking lander cameras. Predictions and measurements of the camera response to three sets of tribars on the reference test chart agreed sufficiently close so that any appreciable image contrast degradation caused by a camera problem can be simulated by the computer program.

Predictions of the picture quality of cones were compared with experimental results for a wide variety of cone slopes and illumination and viewing geometries. The comparison provided consistently good agreement within the accuracy to which experimental data could be quantitatively reduced. The experimentally obtained signal-to-noise ratios of cone pictures depended somewhat on subjective judgments and tended to be slightly higher than the predicted signal-to-noise ratios. However, the variations of predicted and experimental signal-to-noise ratios agreed closely for all variations in cone slope and illumination and viewing geometry.

This good agreement between predictions and experimental results must be credited in part to the Meador-Weaver illumination scattering function

that was used to describe the reflection characteristics of the material used to cover the cones. The illumination scattering function that will actually be encountered at the landing sites on Mars is, of course, less certain. This uncertainty suggests that the dependence of picture quality on lighting and viewing geometry should be investigated for a wide range of reasonable illumination scattering characteristics to establish a sound basis for determining the preprogramed lander commands that automatically direct camera operations during the first few days on Mars. The Meador-Weaver illumination scattering function lends itself readily to this task since it describes the diffuse reflectance of natural materials as a function of their physical properties.

APPENDIX A

PERFORMANCE CHARACTERISTICS OF THE LABORATORY FACSIMILE CAMERA

Although the laboratory facsimile camera differs greatly from the Viking facsimile camera in many design details, it can closely simulate those performance characteristics of the Viking camera which are important to this investigation. This appendix presents a general description of the laboratory camera design, and a detailed description of its performance characteristics when adjusted to simulate the Viking camera performance.

General Description

A basic block diagram of the laboratory facsimile camera is shown in figure 9. Radiation from the scene is reflected by the scanning mirror, captured by the objective lens which has an adjustable aperture, and projected onto a plane which contains the photosensor aperture. The photosensor - in this case a silicon photodiode - converts the radiation falling on the aperture into an electrical current. As the mirror rotates, the imaged scene moves past the aperture permitting the aperture to scan vertical strips. The camera rotates in small steps between vertical line scans until the entire scene of interest is scanned.

The instantaneous field of view is determined by the photosensor aperture size and distance from the lens. Different instantaneous fields of view can be obtained by inserting different modules which consist of a photosensor aperture, photosensor, and preamplifier.

The mirror line-scan motion is directly controlled by a servo, which, in turn, is synchronized to a clock pulse rate. An important part of the servo-control is an accurate mirror position sensor (optical encoder) which has three functions: (1) it aids the servo-control to achieve a linear mirror scan synchronously with the clock rate, (2) it allows the selection of any vertical field of view of the scan (i.e., of an image frame), and (3) it provides pulses for sampling the video signal. Use of these servo-derived pulses (rather than the clock pulse) for sampling the video signal allows the photogrammetric accuracy along the line scan direction to be a function only of the accuracy of the mirror position sensor, and to be independent of small deviations from a constant mirror-scanning velocity.

Immediately after each vertical line scan of the scene, a pulse is sent from the mirror position sensor to the azimuth rotation and filter wheel logic controls. In the broad-band imaging modes, the filter wheel is commanded to position an unfiltered opening over the photosensor aperture, and the azimuth drive (which consists of a steppermotor and harmonic gear) is commanded to advance at the end of each line-scan by a selectable interval (in 0.011 degree steps). In the narrow-band imaging mode, the filter wheel is commanded to rotate a different filter (out of three) over the photosensor aperture after every line scan, and the azimuth drive is commanded to advance after every third line scan.

As shown in figure 10, the photosensor signal current is amplified using a different gain ($R_f G = R_f R_2 / R_1$) for each channel: high-resolution, survey, blue, green, and red. The dark signal voltage (i.e., the voltage level when the mirror is facing the blackened inside of the camera), is integrated by the drift control circuit and then subtracted from the signal.

Additional voltage levels can be subtracted from the signal by a programmable digital-to-analog converter. The resultant signal is then further amplified by a programmable gain amplifier and bandwidth-limited by a low-pass filter. The programmable offsets and gains permit the camera to function with selectable dynamic ranges as illustrated in figure 11. The filter provides adjustable bandlimiting of noise and signal prior to digital sampling.

Performance Characteristics

The performance characteristics of the laboratory camera, which are important to this investigation, are the transfer functions of optics and video electronics and the mirror scanning rate. Most of these characteristics are listed in Table A-1. In addition, figure 12 presents the relative responsivity of the photosensor, figure 13 the transmittance of the color filters, figure 14 the frequency response of the photosensor preamplifier, and figure 15 the frequency response of the adjustable filter used to bandwidth-limit the video signal.

The linearity of the video amplification and processing circuits falls within ±1.0 percent of an ideal straight line for all gain settings over the operating range extending from 0 to 5 V. The accuracy of the offsets is within ±5 mV of the stated value. Exact values for gain and offset are listed in figure 11. The sample and hold circuit used for drift control has a holding accuracy of 0.5 mV/sec.

TABLE A-I
LABORATORY FACSIMILE CAMERA CHARACTERISTICS

Characteristics	Low-Resolution	High-Resolution
Instantaneous field of view, β , deg	0.132	0.044
Mirror reflectance, r_m	0.84	0.84
Lens aperture diameter, D , cm	1.0	1.0
Lens focal length, f , cm	5.5	5.5
Lens transmittance, τ_λ	0.9	0.9
Photosensor aperture diameter, D_a , cm	0.0124	0.0043
Photosensor peak responsivity, R_p , A/W	0.34	0.27
Photosensor-preamplifier feedback resistor, R_f , ohm	0.92×10^9	0.88×10^9
Signal equalization amplifier gain, G_1	Survey: 1.56 Red: 15 Green: 36 Blue: 193	17.5
Picture elements per line	512	512
Field of view per frame		
elevation, deg	67.584	22.528
azimuth, deg; min; max	0.132; 360	0.044; 360
Elevation scan rate, χ_s , deg/sec	520	520
Azimuth stepping rate, deg/sec	Survey: 0.132 Color: 0.044	0.044

APPENDIX B

IRRADIANCE CHARACTERISTICS OF LIGHT SOURCE

Two types of light sources were used in this investigation: National Bureau of Standard (NBS) lamps and a spotlight. The former were used for all absolute radiometric measurements, and the latter for most image quality studies.

NBS Lamp

The NBS light sources are commercial G.E. type DXW-1000-watt lamps that have a tungsten coiled-coil filament enclosed in a 0.95 cm diameter and 7.6 cm long fused silica envelope, which also contains a small amount of iodine. The lamps' color temperature range from 3000°K to 3050°K for a dc current of 7.9 A. Each lamp is supplied by the National Bureau of Standards with calibration data. Figure 16 presents typical spectral irradiance data at a distance of 50 cm; the inverse-square law may be used to calculate the spectral irradiance at distances beyond 50 cm.

Spotlight

The spot light is a 10 KW tungsten lamp with a 61 cm diameter Fresnel lens. It is supplied with rectified 3 phase, 120 V power, and has an effective color temperature of approximately 3200°K at the rated power. However, the following procedure was used to adjust the spotlight to a better known spectral irradiance: A grey reflectance card was first illuminated by a NBS light source and scanned by the laboratory facsimile camera in the repeated line scan mode, alternating the red, green and blue channel, and the gains of the three channels were adjusted until their outputs

were equal. The same grey reflectance card was then illuminated by the spotlight and scanned again by the facsimile camera as before, and the spotlight current was adjusted until the three color channel outputs were the same.

The spotlight optics can be adjusted continuously from spot to flood position. In the full-spot position, the irradiance is concentrated toward the optical centerline and drops off rapidly with distance from the center line. In the full-flood position, the irradiance is spread over a circular area of about 76 cm diameter with +5 percent variations in magnitude. For a setting of 5.5 (near the full-flood position) the irradiance at a distance of 148 cm (as used during most tests) is 1.67 times the irradiance of the NBS lamp EPI 1556 at a distance of 50 cm.

APPENDIX C

REFERENCE TEST CHART CHARACTERISTICS

A picture of the reference test chart (RTC) is shown in figure 17. The paint surfaces consist of 11 grey reflectance patches, three color patches, and three sets of tribar patterns.

Properties of the RTC which are of concern to this investigation are normal reflectance (reflectance at zero illumination and emission angle), illumination scattering function, and tribar dimensions. The normal reflectances of the grey patches are given in Table C-I. Curves of the normal spectral reflectance of the color patches are shown in figure 18. The illumination scattering function for all patches is assumed to be Lambertian (i.e., cosine dependence on illumination angle and no dependence on emission angle). The widths of the individual bars in the tribar patterns are given in Table C-I.

All data presented here for the RTC are preliminary. Evidence exists that significant deviations occur from these nominal values for reflectance, illumination scattering function, and bar widths. These deviations may account for some of the differences between predictions and measurements that have been encountered. Measurements of RTC characteristics have also revealed target-to-target variations. The specific RTC used for measurements must therefore be identified. The serial number for this chart is 15.

TABLE C-I

REFERENCE TEST CHART CHARACTERISTICS

Grey Patch Reflectances		Tribar Widths	
Patch Number	Reflectance	Tribar	Width, mm/λp
1	.11	Large	6.4
2	.15	Medium	3.3
3	.20	Small	2.2
4	.25		
5	.30		
6	.35		
7	.40		
8	.45		
9	.50		
10	.60		
11	.79		

APPENDIX D

THE ILLUMINATION SCATTERING FUNCTION OF A PARTICULATE SURFACE OF COLORADO BASALT

Meador and Weaver (ref. 2) have proposed an illumination scattering function that describes the diffuse reflectance of particulate surfaces as a function of their physical properties (particle albedo, size, and packing density). This appendix presents this function, the geometrical relationships necessary to use it in the prediction program, and the pertinent scattering and physical properties of the Colorado basalt surface used in experimental image quality studies.

The Meador-Weaver Illumination Scattering Function

The scattering function given by Meador and Weaver is (ref. 3)

$$\phi(\iota, \varepsilon, g) = \frac{\cos \iota}{(1 + a_0 + a_1)(\cos \iota + \cos \varepsilon)} \left[(1 + a_0 \cos g) f(\iota, \varepsilon, g; a_2) (D-1) + a_1 (\cos \iota + \cos \varepsilon) \right]$$

where ι is the angle of incidence, ε the angle of emission, g the phase angle, and a_0 , a_1 , a_2 are empirical parameters that contain information about the surface. The factor $f(\iota, \varepsilon, g; a_2)$ is given by

$$f(\iota, \varepsilon, g; a_2) = e^{\mu-\nu} + \nu \int_0^1 \exp \left\{ \mu - \frac{\nu}{6\pi\xi} \left[3\pi(2\xi-1)x + 6x \sin^{-1}x + 2(2+x^2)(1-x^2)^{1/2} \right] \right\} dx$$

Results from this function should be used only for values $f(\iota, \varepsilon, g; a_2) \geq 1$;

all other values should be replaced by $f(\iota, \varepsilon, g; a_2) = 1$. The parameters μ , ν , and ξ are given by

$$\mu = \frac{4a_2 (1 + \cos g)}{3 \sin g}$$

$$\nu = \frac{\pi a_2 (\cos \iota + \cos \varepsilon) [\cos \gamma + \cos (g-\gamma)] \cos \kappa}{\sin g \cos \iota \cos \varepsilon}$$

$$\xi = \frac{(\cos \iota + \cos \varepsilon) \cos \gamma \cos (g-\gamma) \cos \kappa}{[\cos \gamma + \cos (g-\gamma)] \cos \iota \cos \varepsilon}$$

The parameter κ is the angle between the surface normal and the scattering plane (the plane containing the incident and emission directions), and γ is the angle between the incident direction and the projection of the surface normal on the scattering plane. The function $\phi(\iota, \varepsilon, g)$ is normalized to unity at $\iota = \varepsilon = 0^\circ$.

The parameters a_0 , a_1 , and a_2 are empirical parameters which relate certain physical properties of a surface to its scattering properties. While precise quantitative relationships between a_n and the physical properties of the surface have not yet been established, approximate relationships have been determined; a_0 and a_1 are related to particle albedo and size distributions of the surface, and a_2 is related to the packing density of the uppermost particles comprising the surface. A more detailed description of these relationships as summarized from ref. 3 is given by Table D-I below.

Table D-1 - Scattering and Physical Properties of a Surface
Related to a_n Parameters

a_n	Range of a_n	Scattering Property	Physical Property
a_0	-1 to +1	$a_0 < 0$ forward scattering	small transmitting particles
		$a_0 = 0$ isotropic	
		$a_0 > 1$ backscattering	large opaque particles
a_1	0 to ∞	$a_1 = 0$ single scattering	large particles with low albedos
		$a_1 \gg 0$ multiple scattering	small particles with high albedos
a_2	0 to 1	$a_2 \approx 0$	loosely packed
		$a_2 \approx 1$	tightly packed

Geometrical Relationships

The two angular variables κ and γ in the Meador-Weaver function and the angles ι , ϵ , g , and θ used in the prediction program are related as follows:

$$\sin \kappa = \frac{\sin \iota \sin \epsilon \sin \theta}{\sin g} \quad (D-2)$$

$$\sin \gamma = \frac{\sin \iota (\cos \epsilon \sin \iota - \cos \theta \cos \iota \sin \epsilon)}{\cos \kappa \sin g} \quad (D-3)$$

Properties of the Material Used for Experiments

A surface of Colorado basalt (mafic latite porphyry) with a particle size range of 150 to 300 micrometers and a mean particle size of 180 micrometers was used for the experimental image quality evaluations. The

scattering function of this surface has been measured by Meador and Weaver (ref. 3) for coplanar values of incident and emission directions. Values of a_n were determined iteratively using equation (D-1) to fit their experimental data. The values of a_n were determined to be

$$a_0 = -0.4$$

$$a_1 = 0.28$$

$$a_2 = 0.32$$

The validity of using the Meador-Weaver scattering function for non-coplanar geometries of incident and emission directions has not yet been proven for the Colorado basalt surface.

The albedo of the Colorado basalt surface was measured relative to that of Magnesium Carbonate ($MgCO_3$) with a light source having a color temperature of $3000^{\circ}K$ and an unfiltered silicon photosensor. The albedo of $MgCO_3$ is approximately constant over the silicon photosensor responsivity range, so that for this particular condition the albedo of basalt may be taken as

$$\rho_b = \rho_{MgCO_3} \frac{\int S(\lambda) \rho_b(\lambda) \tau_c(\lambda) R(\lambda) d\lambda}{\int S(\lambda) \rho_{MgCO_3}(\lambda) \tau_c(\lambda) R(\lambda) d\lambda} = (0.97)(0.20) = 0.19$$

where the factor 0.20 is the measured ratio.

REFERENCES

1. Huck, F. O.; Jobson, D. J.; Taylor, E.J.; and Wall, S. D.: Formulation of Image Quality Prediction Criteria for the Viking Lander Camera. NASA TM X-2802, September 1973.
2. Meador, W. E.; and Weaver, W. R.: A Photometric Function for Diffuse Reflection by Particulate Materials. Prospective NASA TN.
3. Weaver, W. R.; Meador, W. E.; and Wood, G. P.: Values of the Photometric Parameters of Mars and Their Interpretation. NASA TM X-71949, May 1974.

TABLE I

COMPARISON OF PREDICTED AND MEASURED REFERENCE TEST CHART DATA

Reference Test Chart Characteristics	Hi-Res 1			Hi-Res 2			Camera Channels Survey			Red			Green			Blue			Aver. %E
	P	M	%E	P	M	%E	P	M	%E	P	M	%E	P	M	%E	P	M	%E	
Grey patch: 40% reflectance	5.34	5.25	2	5.44	5.29	3	5.58	5.26	6	4.78	4.85	2	4.97	4.65	7	5.41	5.12	6	4
Color patches:																			
Red	7.84	6.89	13	7.99	7.07	12	8.18	6.95	16	7.35	6.83	7	.841	1.04	21	.64	.79	21	15
Green	5.46	5.52	1	5.57	5.52	1	5.71	5.46	4	1.38	1.77	25	2.50	2.57	3	.97	1.90	6	7
Blue	8.55	8.05	6	8.72	8.18	6	8.93	8.06	10	2.91	3.08	6	1.38	1.45	5	5.98	5.23	13	8
Tribars:																			
12.6mm/λp	4.74	4.59	3	4.71	4.36	8	4.18	3.89	7	3.58	3.06	16	3.73	3.13	17	4.05	4.21	4	9
6.6mm/λp	2.97	2.00	39	1.35	1.47	9	.53	.38	33	.44	.24	.70	.46	.26	56	.49	.38	25	39
4.4mm/λp	.71	.35	68	-.51	-.31	49	-.57	-.38	40	-.49	-.57	15	-.52	-.37	34	-.56	-.89	46	42

P = Prediction

Percentage Error:

- = Phase reversal

M = Measurement

$$\%E = \frac{|P - M|}{\frac{1}{2}(P+M)} \cdot 100$$

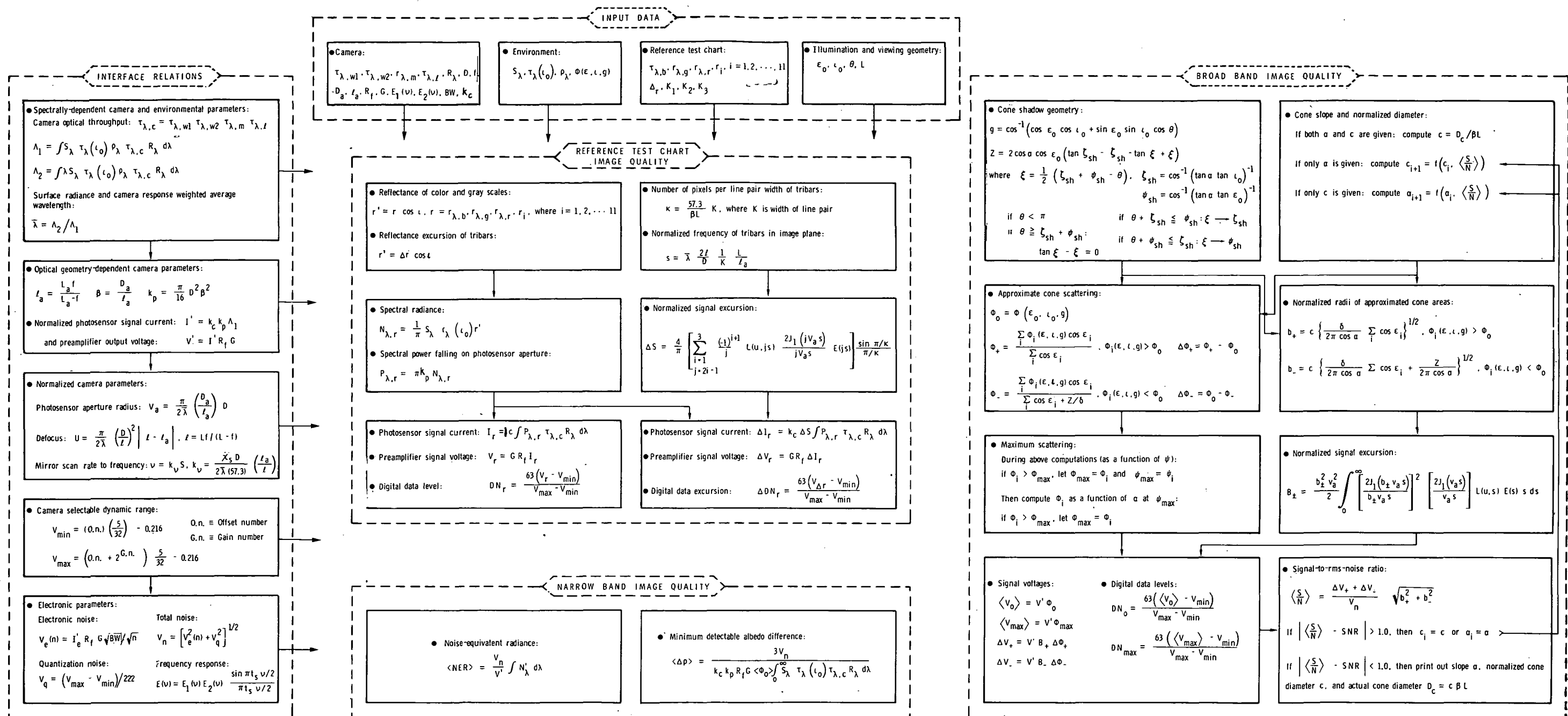
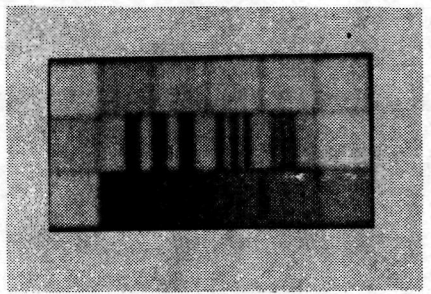
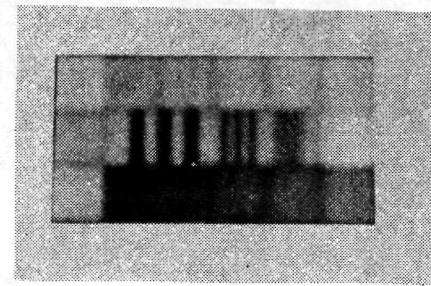


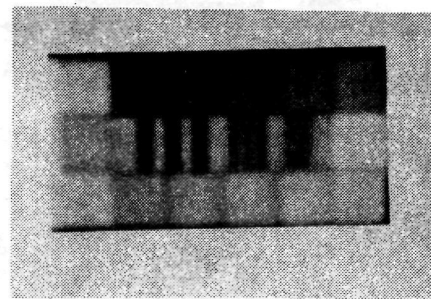
Figure 1.- Block diagram of computer program.



Survey



Hi-Res 2



Hi-Res 1

Figure 2.- Three pictures of a reference test chart located 1.0m from the camera. The Hi-Res 1 and Hi-Res 2 pictures were obtained with an instantaneous field of view of 0.044° and in-focus distances of 1.9m and 2.7m, respectively; the Survey picture was obtained with an instantaneous field of view of 0.132° and in-focus distance of 3.7m.

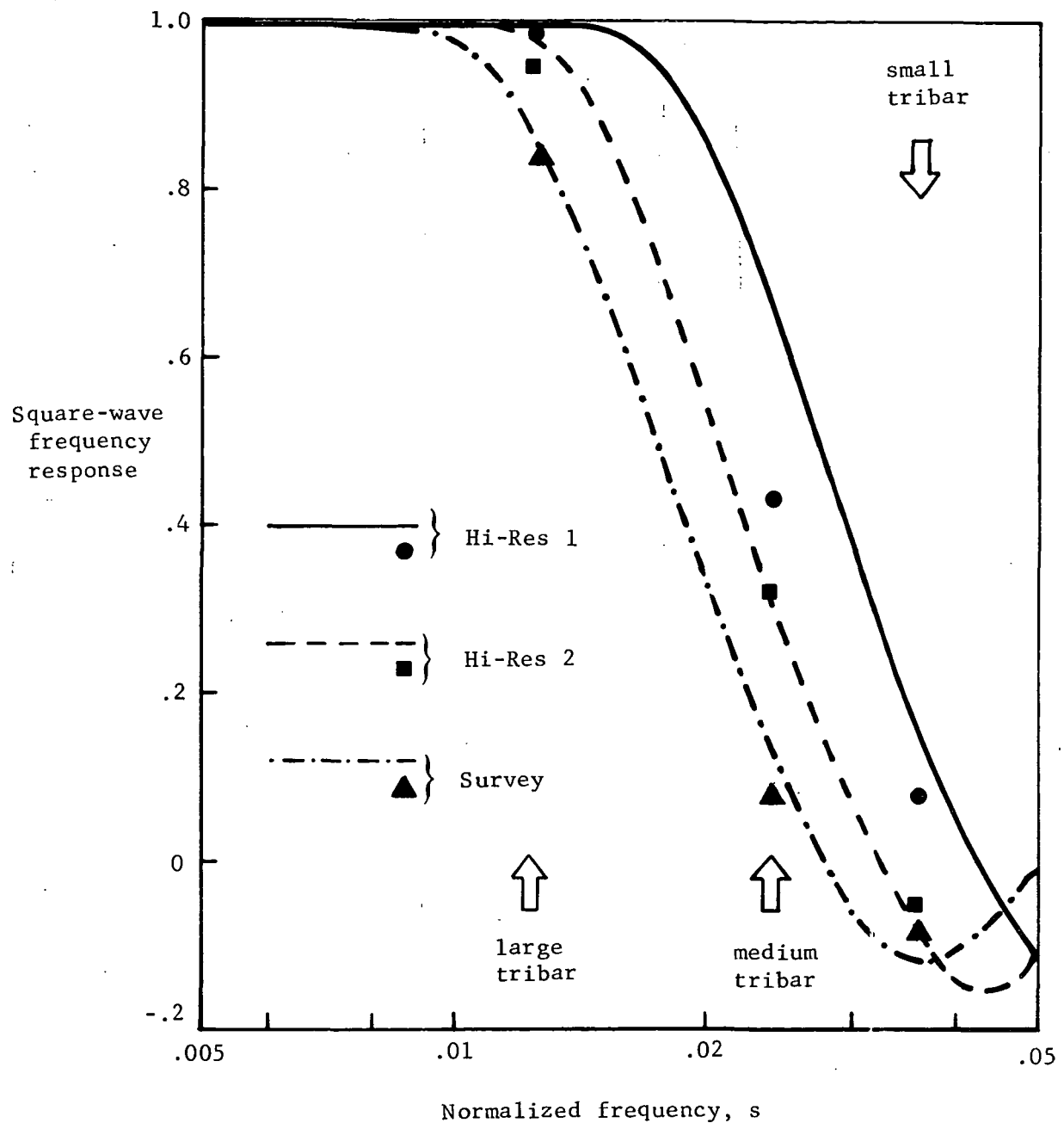


Figure 3.- Predicted square-wave frequency response of the camera for a target located 1.0m away, and normalized tribar contrast measurements.

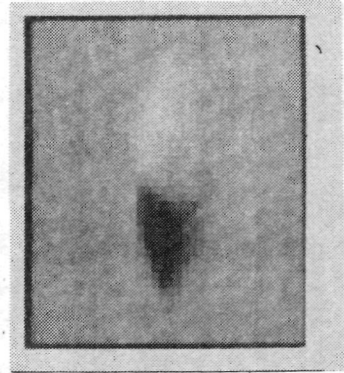


Figure 4.- Typical cone picture and computer printout of data.

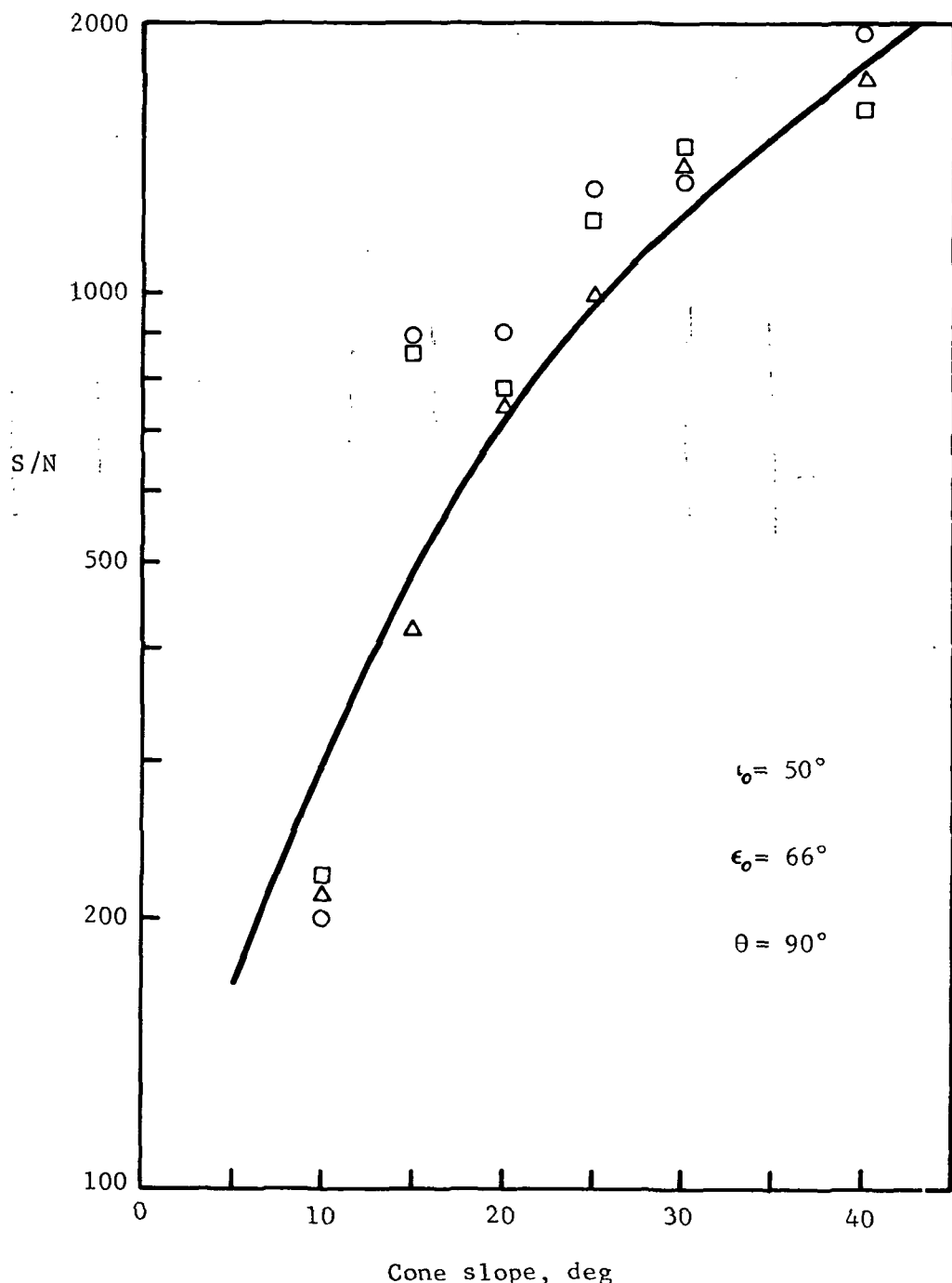


Figure 5.- Comparison of predicted signal-to-noise ratio with measured results independently obtained by three evaluators. The camera Survey mode was used with an in-focus distance equal to the approximately 1.4m distance of the 3cm diameter cones.

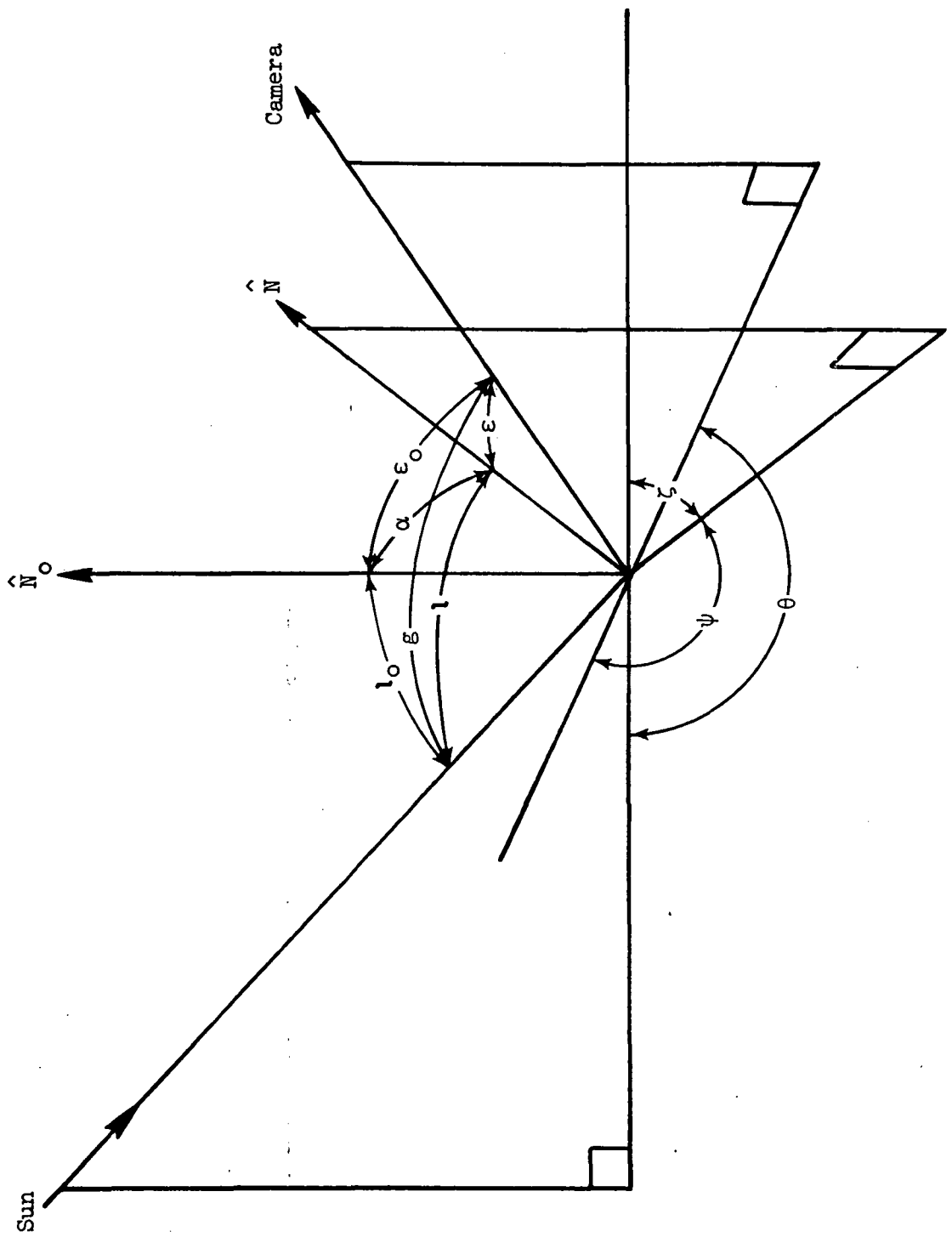
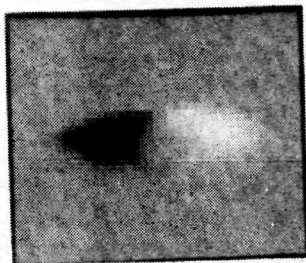


Figure 6.- Illumination and viewing geometry.



Azimuth angle, θ	Cone parameter	Pred.	Meas.
90°	N+	130	181
	N-	203	194
	S/N	1695	1901



45°	N+	186	238
	N-	147	157
	S/N	1382	1565



180°	N+	65	95
	N-	269	276
	S/N	1456	1842

Figure 7.- Predicted and measured signal-to-noise ratios for a cone with a 3cm diameter base and a 25° slope. Also given are the number of pixels contained in the brighter (N_+) and darker (N_-) than background part of the cone. The camera Hi-Res mode was used with an in-focus distance equal to the 1.4m distance of the cones. The illumination and viewing angles were $\iota_0 = 70^\circ$ and $\epsilon_0 = 60^\circ$, respectively.

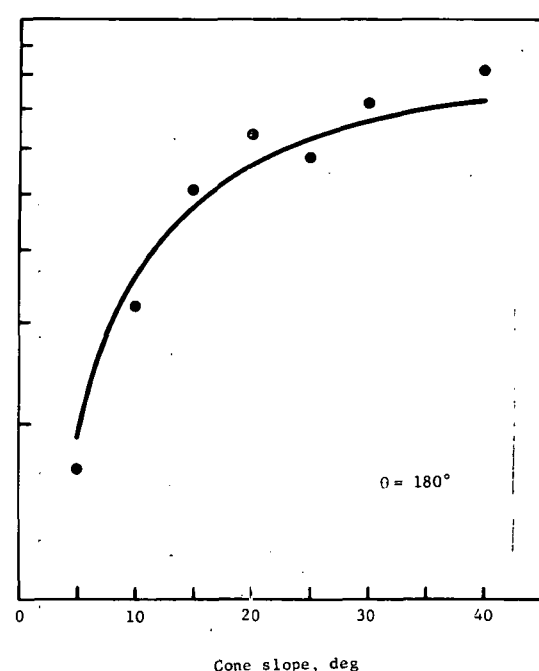
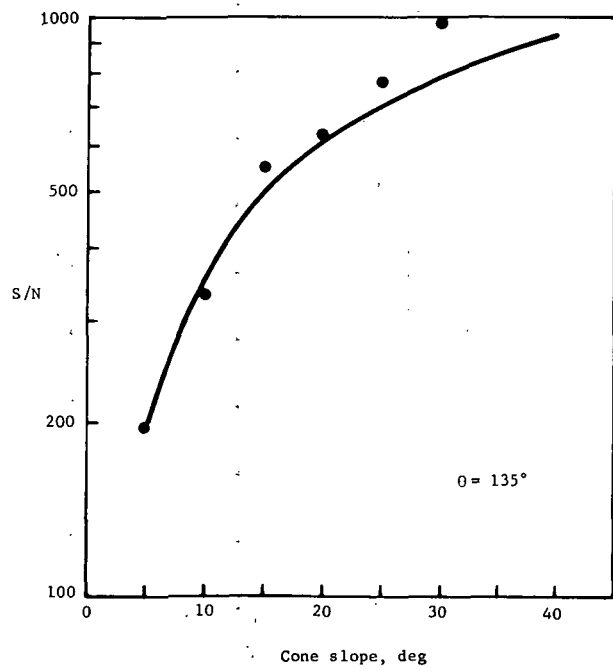
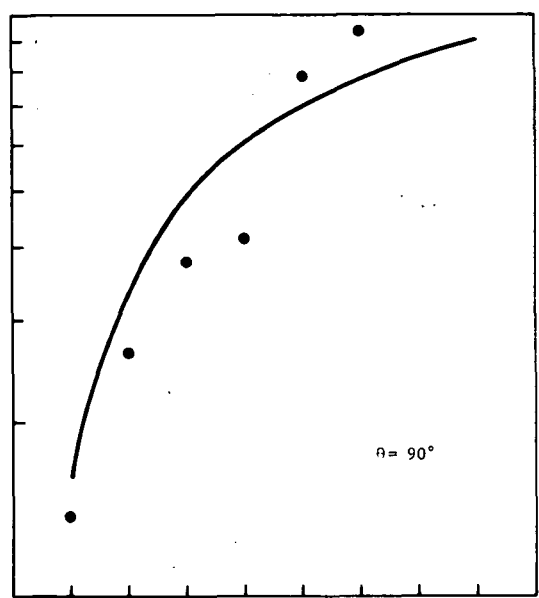
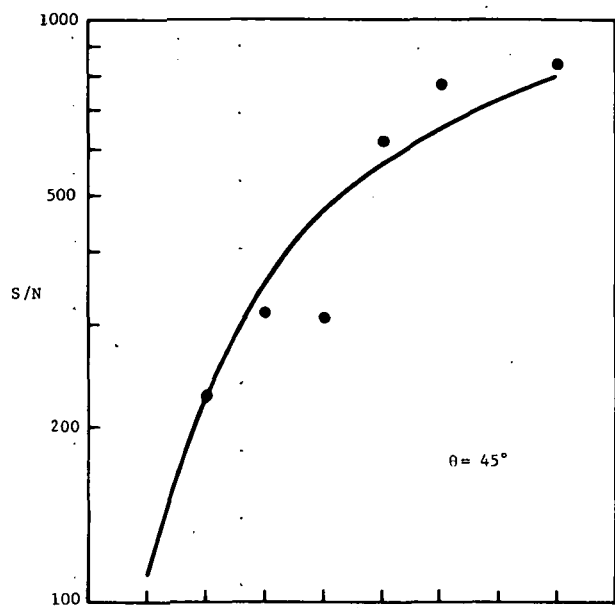


Figure 8.- Predicted and measured signal-to-noise ratios for cones with a 3cm diameter base and various slopes. The camera Survey mode was used with an in-focus distance equal to the approximately 1.4m distance of the cones. The illumination and viewing angles were $\iota_0 = 70^\circ$ and $\epsilon_0 = 60^\circ$, respectively.

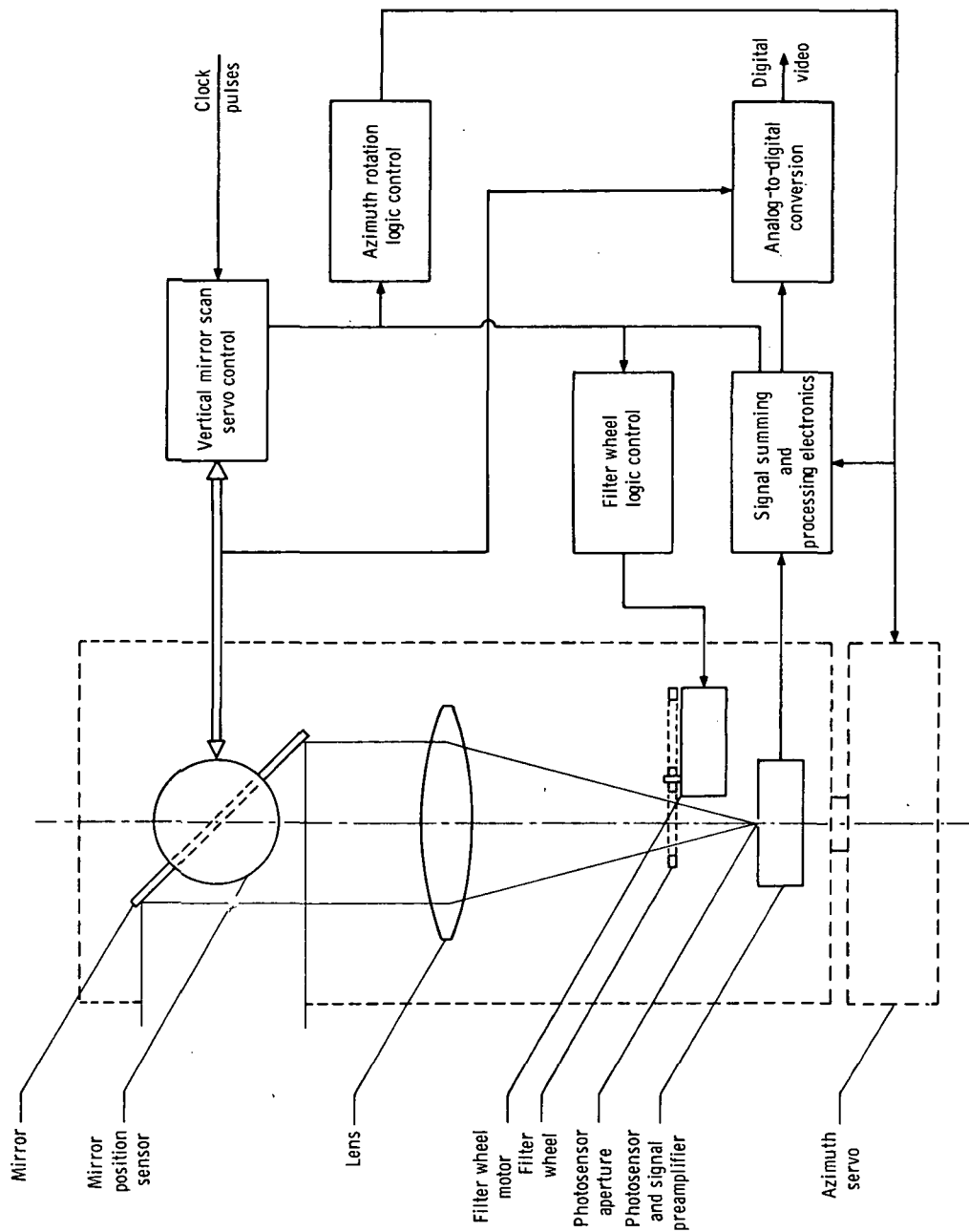


Figure 9.- Block diagram of laboratory facsimile camera.

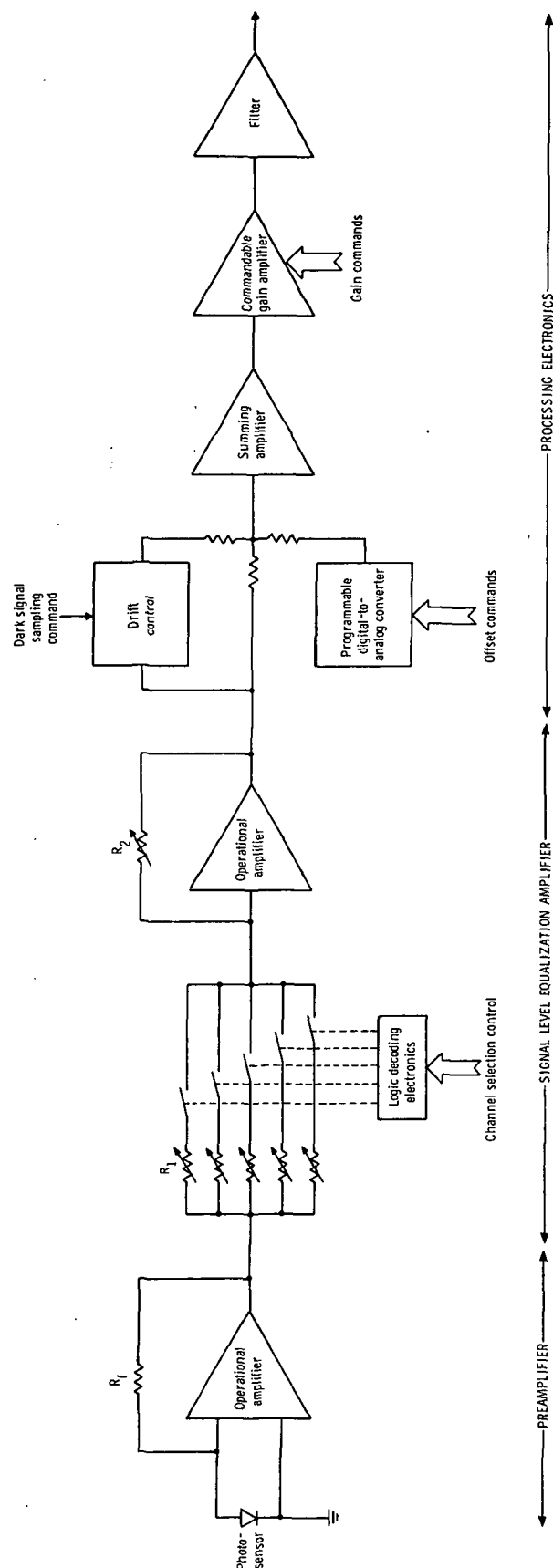
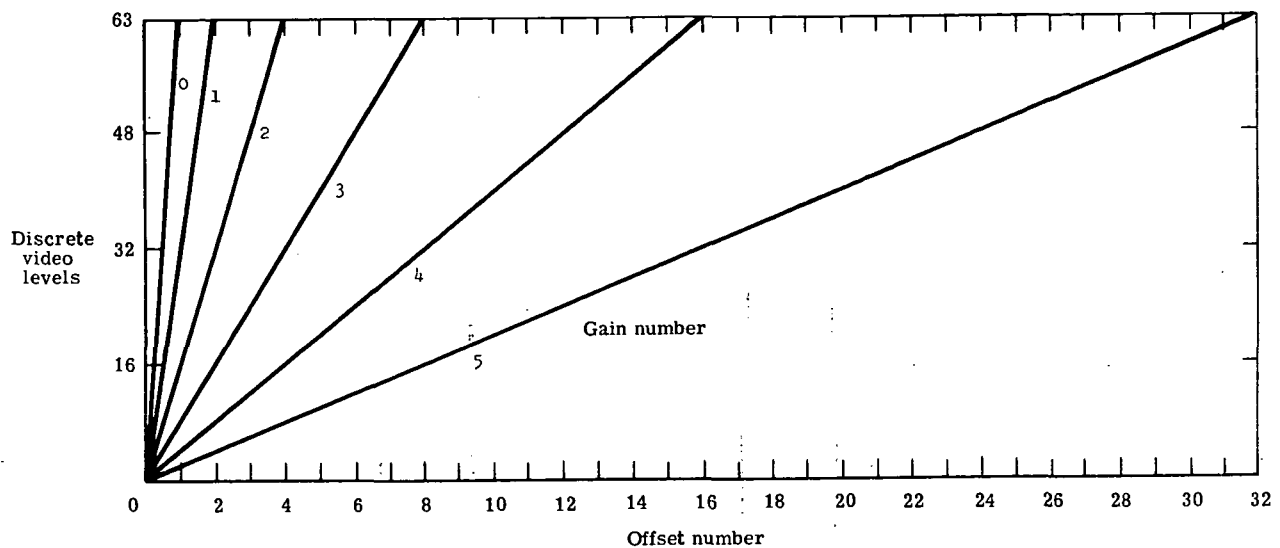


Figure 10.- Block diagram of analog video electronics.



Offset Number	Offset Voltage	Offset Number	Offset Voltage
0	.000	16	2.499
1	.156	17	2.655
2	.312	18	2.811
3	.469	19	2.967
4	.625	20	3.124
5	.781	21	3.280
6	.937	22	3.436
7	1.094	23	3.592
8	1.250	24	3.748
9	1.406	25	3.904
10	1.562	26	4.061
11	1.718	27	4.217
12	1.875	28	4.373
13	2.031	29	4.529
14	2.187	30	4.686
15	2.343	31	4.842

Gain Number	Voltage Gain
0	32.01
1	16.04
2	7.99
3	4.01
4	2.00
5	1.00

Figure 11.- Selectable gains and offsets.

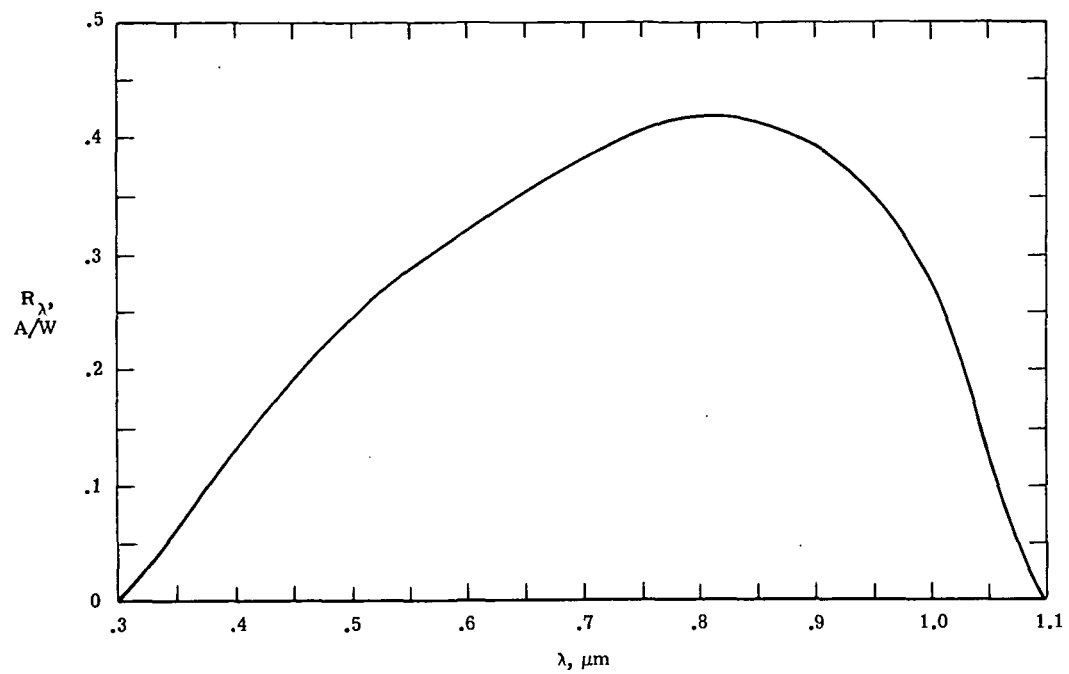


Figure 12.- Responsivity of silicon photodiode.

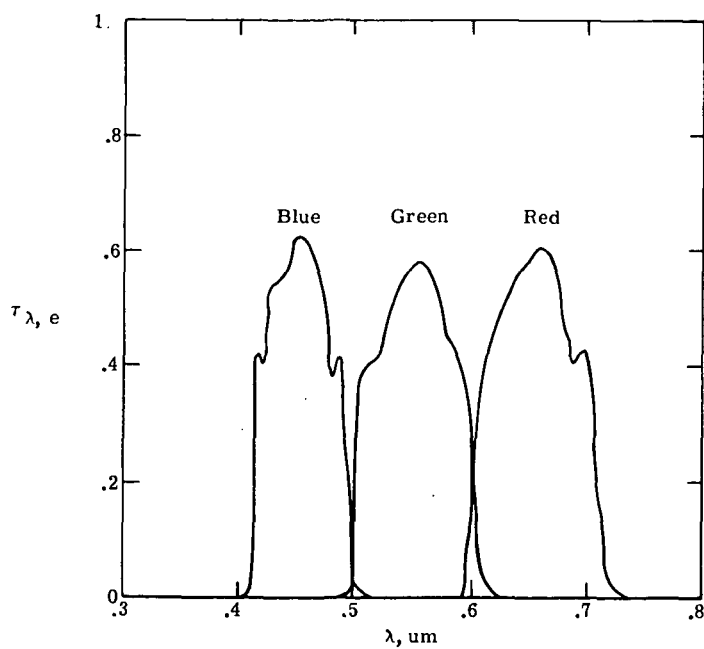


Figure 13.- Transmittance of color filters.

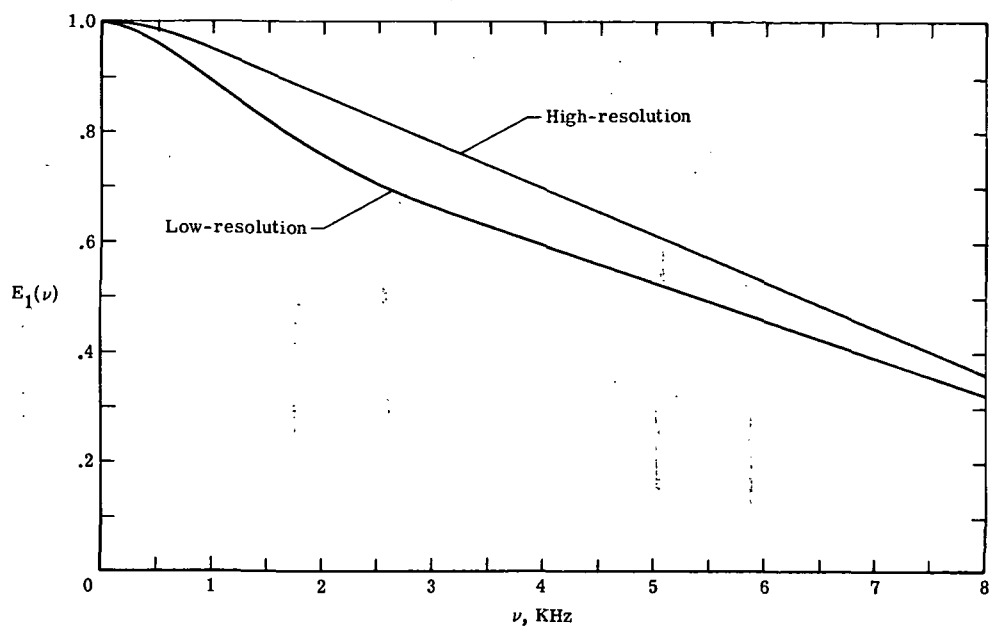


Figure 14.- Frequency response of photosensor preamplifier.

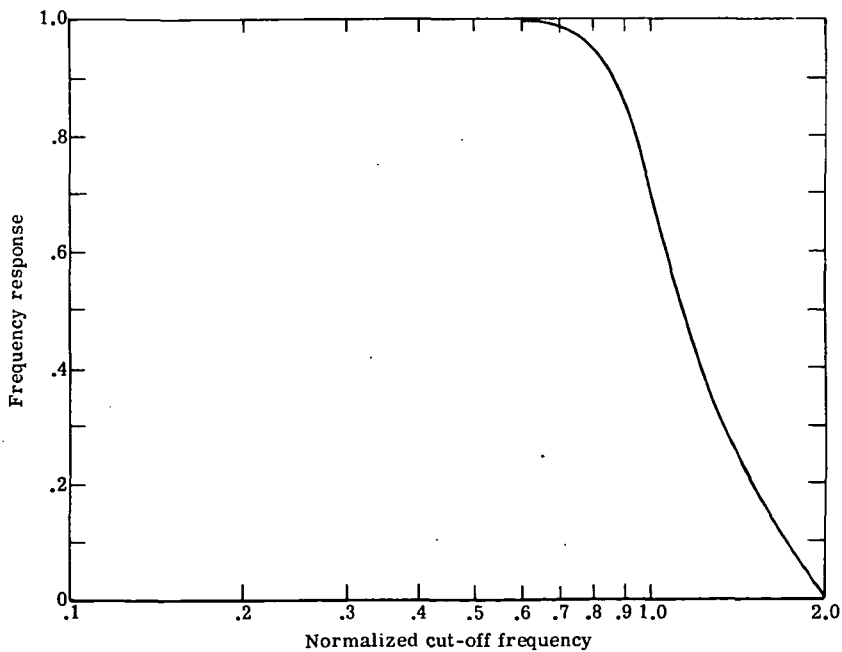


Figure 15.- Frequency response of variable electronic filter.

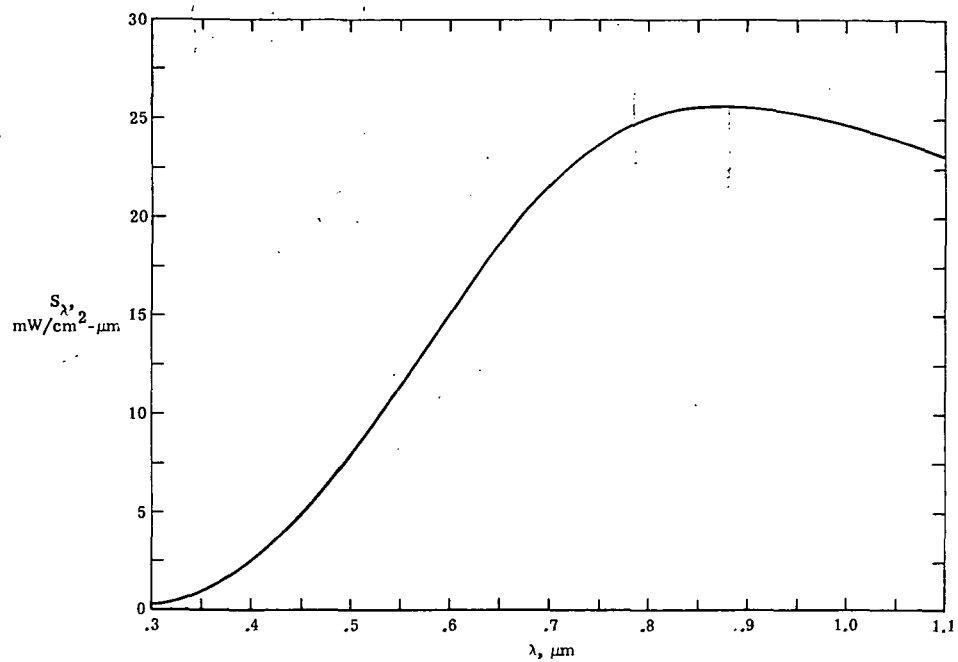


Figure 16.- Typical spectral irradiance of NBS lamp at a distance of 50 cm when operated at 7.9 A.

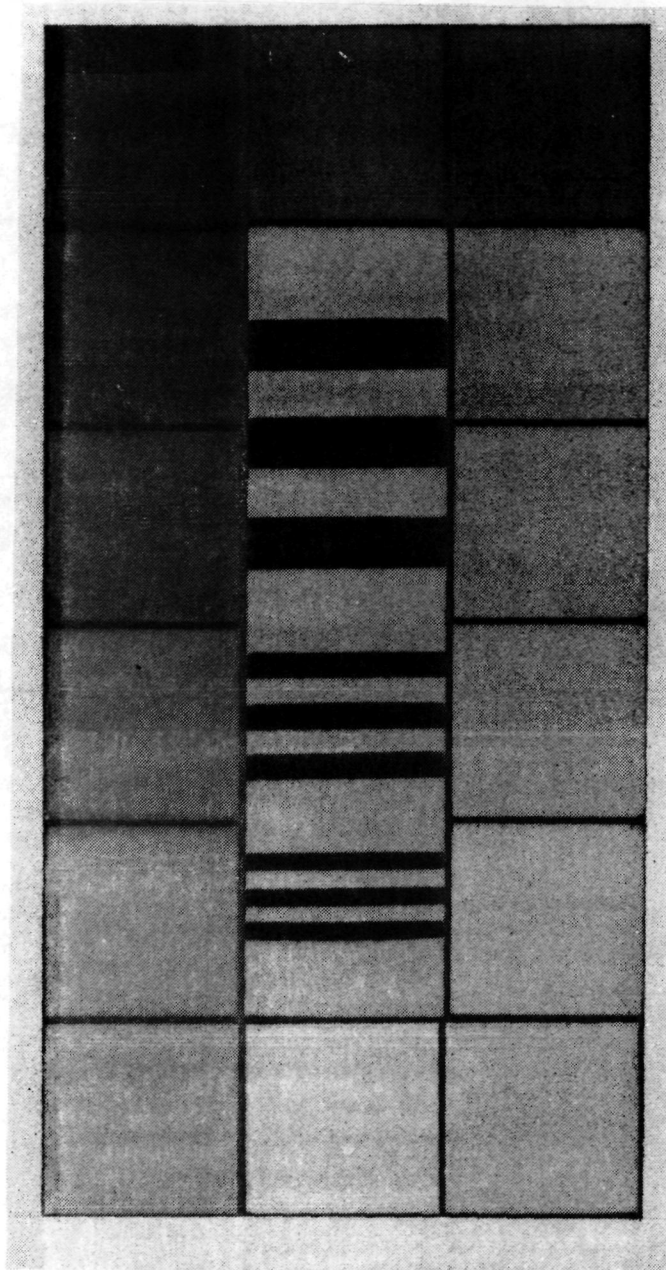


Figure 17.- Reference test chart.

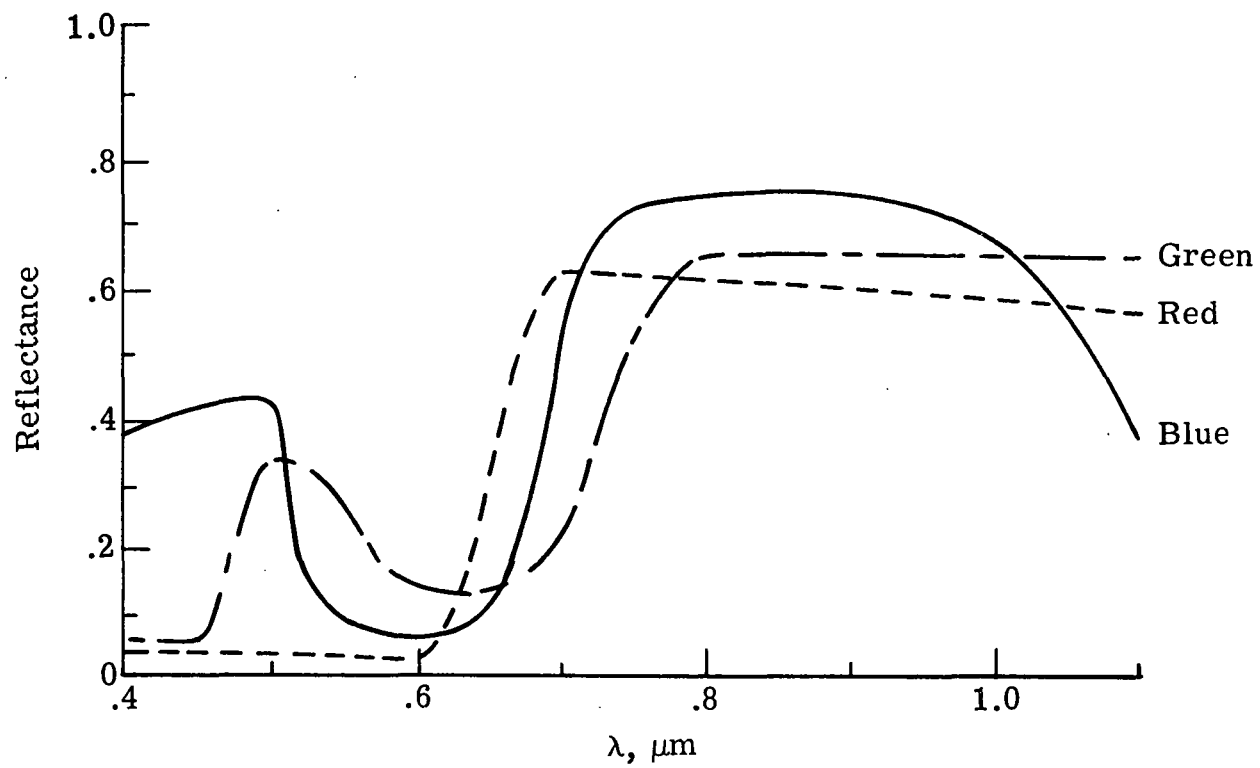


Figure 18.- Spectral reflectances of reference test chart color patches.